Volume 23
Number 13
7 July 2021
Pages 4623-4904

Green Chemistry

Cutting-edge research for a greener sustainable future

rsc.li/greenchem

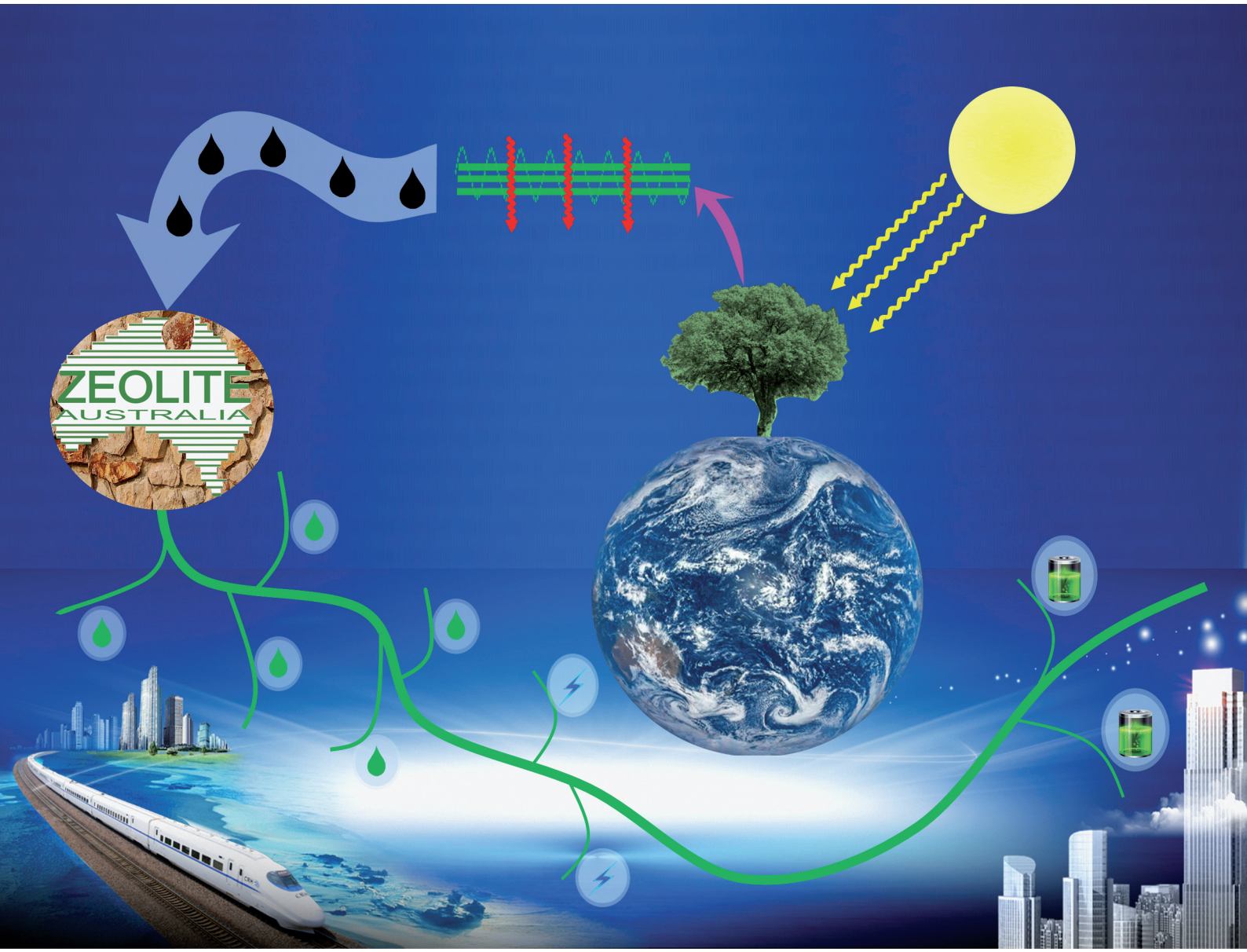

ISSN 1463-9262

ROYAL SOCIETY OF CHEMISTRY

PAPER
Michael Stockenhuber *et al.*
Natural zeolite supported Ni catalysts for hydrodeoxygenation of anisole

Green Chemistry

PAPER

View Article Online
View Journal | View Issue

Check for updates

Cite this: *Green Chem.*, 2021, **23**, 4673

Natural zeolite supported Ni catalysts for hydrodeoxygenation of anisole†‡

Penghui Yan, Eric Kennedy and Michael Stockenhuber *

Received 28th December 2020,
Accepted 19th April 2021

DOI: 10.1039/d0gc04377j

rsc.li/greenchem

Natural and synthetic (BEA, MOR) zeolite-supported nickel (~5 wt%) catalysts were prepared and employed for the hydrogenation of toluene and hydrodeoxygenation of anisole in a continuous-flow reactor. Ni/BEA and Ni/MOR display a higher level of metal dispersion and stronger metal–support interaction compared to the Ni/NZ and Ni/Escott catalysts, resulting in a higher concentration of charge-compensating Ni species and a larger high-temperature reduction peak. The Ni/BEA and Ni/MOR also present a significant mass of low-temperature desorbed H_2 (centred at 150 °C) based on H_2-TPD, suggesting the H species are weakly adsorbed on small Ni clusters. In contrast, the H species were strongly adsorbed by the bulk Ni crystal over Ni/Escott and Ni/NZ, which were desorbed at maxima between 211 and 222 °C. We propose that the strongly adsorbed H species play a crucial role in the hydrogenation of toluene, leading to a significantly higher yield of methylcyclohexane over Ni/Escott and Ni/NZ compared to Ni/BEA and Ni/MOR. Both metal and acid sites are required in the hydrodeoxygenation of anisole. The strong Brønsted acid sites and numerous smaller Ni species over Ni/BEA facilitated the transalkylation of anisole to phenol and methylanisole and subsequently hydrogenolysis of phenol to benzene, followed by the hydrogenation of benzene to cyclohexane.

Published on 14 June 2021. Downloaded on 8/31/2021 9:38:13 PM.

1. Introduction

The depletion of readily accessible, traditional feedstocks of liquid fossil fuels and rapidly increasing demand for renewable oil and green chemicals (such as green BTX), is creating strong incentive for the development of non-petrochemical derived fuels and chemicals.[1] Biocrude oils, which are derived from the pyrolysis or liquefaction of biomass, are considered to be suitable candidates due to the quantity of biomass available around the world.[2,3] However, bio-oils usually have a high content of oxygen, leading to high acidity, reduced calorific value, high viscosity and decreased thermal stability and thus cannot be directly used as transporting fuels.[4,5] To address these limitations, bio-oils upgrading is required to reduce the oxygen content.

Hydrodeoxygenation (HDO), which employs bifunctional catalysts and hydrogen gas cofeed to remove oxygen from feedstocks, is considered to be an effective method for biocrude oil upgrading.[6,7] Bifunctional catalysts, including supports and active metals, play a pivotal role in the HDO process.[8,9] Noble metals such as Pt, Pd and Ru, which are supported on carbon, Al_2O_3, SiO_2 and zeolites, are commonly employed in the HDO reactions.[10–13] While these catalysts are reported to possess a higher activity compared to traditional HDO catalysts such as NiMoS and CoMoS, their high cost restricts the widespread commercial application of these catalysts.[14] In addition, sulfided catalysts are generally regarded less favourably as a result of product contamination with sulfur. Non-noble metal catalysts such as metallic Ni, Fe, W and Mo or their combinations, supported on zeolites, are also the subject of investigations in HDO reactions, which generally exhibit a high HDO activity.[15–17] Ni–Ga alloy can suppress the hydrogenation of aromatic rings during the anisole hydrodeoxygenation, leading to an increased yield of benzene.[18] Wang[19] investigated the HDO of anisole over Al_2O_3 supported NiMo, MoP and Ru catalysts. NiMo with moderate hydrogenation activity enhanced the transalkylation reaction *via* a partial hydrogenation reaction. The transalkylation and hydrogenolysis of anisole to BTX was also facilitated by zeolites (ZSM-5, BEA) supported Ni–Fe alloy and low pressure.[20] The pore size of the supports plays an important role in HDO reactions. Gamliel[21] observed Ni supported on modified mesoporous USY zeolite was more effective for HDO of anisole than the Ni/USY catalyst with higher micropore volume.

Natural, untreated zeolites, which are abundant and inexpensive compared to synthetic zeolites (such as BEA, MFI), are rarely applied in the HDO reactions. The natural zeolites

Chemical Engineering, School of Engineering, University of Newcastle, Callaghan, NSW, 2308, Australia. E-mail: michael.stockenhuber@newcastle.edu.au

†This paper is dedicated to the memory of Mr Greg Stephen from Zeolites Australia, a lifelong supporter of Australian zeolite science.

‡Electronic supplementary information (ESI) available. See DOI: 10.1039/d0gc04377j

Published on 14 June 2021. Downloaded on 8/31/2021 9:38:13 PM.

present crystalline hydrated aluminosilicates with framework structures such as clinoptilolites and chabazites.[22] In addition, the natural zeolites are considered "green" as they are not manufactured unlike synthetic zeolites, which require hazardous substances (such as organic structure-directing agents) during the synthesis.[23]

Natural zeolites, which can be activated by water or ion exchange, have been used for hydrocarbon cracking or isomerization reactions.[24–26] Due to their typical characteristics, especially their high content of acid sites and desirable textural properties,[22,27] natural zeolites have potential application in the upgrading of biocrude oil. In addition, natural zeolites usually contain elevated quantities of Fe species which play an important role in C–O cleavage,[28,29] and therefore it is expected that the natural zeolites supported Ni catalysts could exhibit high activity towards the biocrude oil deoxygenation.

In this study, two natural zeolites (NZ and Escott) and two synthetic (BEA and MOR) zeolites supporting nickel (~5 wt%) were investigated. The properties of natural zeolites and catalysts were studied by XRF, FTIR, TPD, TPR, XRD, TEM, XPS, and chemisorption. Meanwhile, hydrogenation of toluene and HDO of anisole were performed to examine the hydrogenation and HDO activities of catalysts.

2. Experimental

2.1. Catalyst preparation

Two natural zeolites NZ (Si/Al = 5.0) and Escott (Si/Al = 5.7) were supplied by Zeolite Australia Limited (234 Escott Road, Werris Creek, NSW, Australia). H-BEA (Si/Al = 12.5) and H-MOR (Si/Al = 10) zeolites were obtained from Zeolyst International (Conshohocken, US). The Escott and NZ (8 g) raw materials were ion exchanged with 200 mL of ammonium nitrate (NH_4NO_3) (0.5 M) at 60 °C for 24 h to generate acid sites. This ion exchange procedure was repeated 3 times. The wet solids were then filtrated and dried at 120 °C overnight and calcined at 500 °C for 4 h. A pre-determined mass of nickel nitrate hexahydrate ($Ni(NO_3)_2{\cdot}6H_2O$) was dissolved in appropriate distilled water and then impregnated on NZ, Escott, BEA and MOR supports. The final mixtures were dried at 50 °C for 12 h, followed by calcination in air at 500 °C for 4 h. The term 'pre-reduced' represents the catalysts which were reduced by H_2 (50 mL min^{-1}) at 500 °C for 3.5 h.

2.2. Catalyst characterisation

Nitrogen adsorption–desorption was carried out at −196 °C in a Micromeritics Gemini surface area analyser to determine the surface area and pore properties of catalysts. Prior to nitrogen adsorption, the samples were degassed using Micromeritics Vac Prep 061 sample preparation device. The *t*-plot and Barrett–Joyner–Halenda (BJH) models were used to estimate micro and mesopore volumes, as well as the pore size distribution. The extent of metal dispersion of each catalyst was investigated by volumetric chemisorption. All samples were pre-treated in pure H_2 (100 mL min^{-1}) at 450 °C for 2 h. The chemisorption of carbon monoxide was performed at 35 °C over a pressure range between 30 and 90 mbar, and the total number of gas adsorbed was calculated based on the ideal gas law. Based on the volume of chemisorbed CO, the metal dispersion (D) and average metal particles size (d) were calculated using eqn(1) and (2).[30,31]

$$D = \frac{N_S}{N_t} \times 100\% = \frac{SF \cdot M_W \cdot n \cdot 10^2}{W\,wt\%} \quad (1)$$

$$d(nm) = \frac{\varphi \cdot M_W \cdot \sigma}{D \cdot \rho \cdot N_A} \quad (2)$$

where N_s is the moles of accessible metal, N_t represents moles of total metal content, SF is stoichiometry factor (CO/Ni = 1/1), M_w is formula weight of the particle (g mol^{-1}), n is the mole of active gas adsorbed, wt% represents the weight% of metal in sample, W is the total weight of sample, σ is the atomic cross-sectional area of metal (m^2 per atom), N_A is the Avogadro number, φ is a constant which reflects particle shape (*e.g.* φ is 6 for spheres and cubes), and ρ is the metal particle density (g cm^{-3}).

The X-ray diffraction patterns of catalysts were obtained in a Phillips X'pert Pro diffractometer with Cu Kα radiation. The XRD reflections were recorded in the range of 2θ = 5–90°.

Acid site concentration and the relative strength of acid sites on each catalyst were determined by temperature-programmed desorption (TPD) of ammonia, using an apparatus described in detail elsewhere.[32] The heat of desorption was calculated based on the procedure published by Redhead:[33]

$$\frac{\Delta E_{des}}{RT_{max}} = \ln\frac{\nu_1 T_{max}}{\beta} - 3.64 \quad (3)$$

where ΔE_{des} is the activation energy of desorption, R is the ideal gas constant. The frequency factor is estimated to be constant, $\nu_1 = 10^{13}$ s^{-1}. T_{max} is the temperature at which the desorption rate is a maximum, β is the heating rate.

H_2-TPD experiments were carried out in the same apparatus as the NH_3-TPD measurements. 0.2 g calcined catalyst was reduced in a pure H_2 (50 mL min^{-1}) at 500 °C for 3.5 h. The pre-reduced sample was vacuumed for 1 h at 500 °C then cooled to 50 °C and saturated with 10 mbar H_2. H_2 desorption patterns were obtained from 50 °C to 450 °C at a heating rate of 10 °C min^{-1}. The desorbed H_2 was detected by a mass spectrometer.

Transmission electron microscopy (TEM) imaging was carried out in a JEOL JEM-1200EXII TEM (200 kV) microscope, equipped with an EDXS spectrometer. Samples were prepared using an ethanol dispersion method and placed on a copper grid.

Temperature-programmed reduction (TPR) was performed in a custom-built instrument[8] to determine the reducibility of catalyst. The catalyst was first activated in air (20 mL min^{-1}) at 500 °C for 60 min to remove water and other impurities, followed by cooling to 50 °C. Reduction was carried out using a 2.04 vol% H_2/Ar flow (50 mL min^{-1}) from 50 °C up to 900 °C with a heating rate of 10 °C min^{-1}. The hydrogen consumption

 This journal is © The Royal Society of Chemistry 2021

Published on 14 June 2021. Downloaded on 8/31/2021 9:38:13 PM.

was recorded by TCD. A trap containing dry ice was placed between the reactor and TCD to remove water.

FTIR spectra were recorded with a Bruker Tensor 27 FTIR spectrometer. Self-supporting wafers were prepared by application of a pressure of 5 ton cm^{-2}. The pressed wafer was placed in a sample holder in the centre of a furnace located in the FTIR cell. Prior to the adsorption experiment, the sample was first off-line reduced in pure H_2 (50 mL min^{-1}) at 500 °C for 3.5 h. The pre-reduced sample was then ground and pressed to prepare a wafer, followed by activation at 500 °C by three repeated injections of hydrogen (10 mbar) per evacuation cycles and held at 500 °C for 1 h under vacuum (10^{-7} mbar). The IR spectra of adsorbed NH_3 were recorded at 150 °C with a NH_3 pressure range between 1.0×10^{-4} mbar and 10 mbar. For quantitative analysis of the number of catalytically active sites, the intensities of bands of coordinatively bound ammonia (1575–1649 cm^{-1}) and Brønsted acid sites (1340–1553 cm^{-1}) were quantified using the respective extinction coefficients: 0.11 cm^2 μmol^{-1} for the NH_4^+ band and 0.026 cm^2 μmol^{-1} for the NH_3-L band.[34] The IR spectra of adsorbed H_2 were recorded at 50 °C with a H_2 pressure range between 1.0×10^{-3} mbar and 10 mbar. H_2 and NH_3 were desorbed from the adsorption temperature to 500 °C at a heating rate of 10 °C min^{-1}.

2.3. Catalytic reaction and product analysis

The hydrodeoxygenation reactions were tested in a continuous-flow reactor. Catalyst was charged in the centre of a tubular reactor and held in place with quartz wool. A thermocouple was placed in the middle of the catalyst bed to monitor the reaction temperature. The catalysts were reduced at 500 °C for 3.5 h at a flow rate of 50 mL min^{-1} pure H_2 before the reactivity test. After catalyst pre-treatment, the temperature was adjusted to reaction temperature and the total hydrogen pressure was increased to 4 MPa. The reactant (anisole or toluene) was introduced into the reactor with a HPLC pump.

The liquid products from HDO of anisole were analysed by an Agilent GC-6980 MS *via* a Rtx-200 MS (30 m length, 0.25 mm ID, and 0.5 μm film thickness) column. Helium was used as carrier gas with a sample injection volume of 1 μL and a split ratio of 100 : 1 applied for all samples. Injector and detector were maintained at 220 °C and 285 °C, respectively. The initial oven temperature (40 °C) was held for 5 min, increasing to 250 °C at a rate of 10 °C min^{-1}. The filament detector was turned off during the elution of the injection solvent (CH_2Cl_2). The liquid products (methanol, methyl-cyclohexane, cyclohexane, cyclohexene, cyclohexanol, 1,1′-bicyclohexyl, 2-methoxycyclohexane, anisole, toluene, and phenol) were calibrated by standard chemicals from Sigma-Aldrich, other complex coupling products (notably cyclohexyl-anisole and methylcyclohexyl-anisole), which have similar structures with 1,1′-bicyclohexyl, were calibrated using the same response factor as 1,1′-bicyclohexyl. Gaseous products from the continuous-reactor were analysed *via* an online Varian 490-GC micro gas chromatograph equipped with two columns (10 m PPQ; 15 m 5CB), and a mixture of gaseous components (helium balanced, 2000 ppm methane, 2000 ppm ethane, 2000 ppm ethene, 2000 ppm propane, 2000 ppm propene, 2000 ppm *n*-butane, 2000 ppm isobutene) was used as calibration gas for the Micro-GC.

$$\text{Toluene conversion}(X_{\text{toluene}}) = \frac{\text{toluene in feed} - \text{toluene in products}}{\text{toluene in feed}} \times 100\% \quad (4)$$

$$\text{Anisole conversion}(X_{\text{anisole}}) = \frac{\text{anisole in feed} - \text{ansiole in products}}{\text{anisole in feed}} \times 100\% \quad (5)$$

$$\text{Product yield}(Y) = \frac{\text{carbon mass of product}}{\text{carbon mass of feed}} \times 100\% \quad (6)$$

$$\text{Product selectivity}(S) = \frac{\text{carbon mass of product}}{\text{carbon mass of}(\text{initial feed} - \text{feed after reaction})} \times 100\% \quad (7)$$

The conversion of toluene and anisole was calculated using eqn (4) and (5). Product yield and selectivity were determined by eqn (6) and (7). Product yield was calculated on the basis of the carbon mass.

3. Results and discussion

3.1. Characterisation results

The physicochemical properties of supports and pre-reduced catalysts are summarised in Table 1, with nitrogen adsorption/desorption isotherms displayed in Fig. S1.‡ It is noted that the natural zeolites possess lower pore volume and surface area compared to HBEA. The NZ zeolite shows a higher micropore surface area compared to Escott, indicating a higher number of micropores contained by NZ zeolite. The HMOR exhibits the highest micropore surface area and a similar mesopore surface area with NZ zeolite. Due to the low concentration of pores, Escott and NZ supported Ni catalysts display a significantly lower metal dispersion and larger Ni particle distribution compared to Ni/BEA and Ni/MOR. In addition, NZ and Escott zeolites contain a low amount of Fe (~1.0%).

The X-ray diffraction patterns of supports and pre-reduced catalysts are shown in Fig. 1. The metallic Ni (1 1 1), (2 0 0) and (2 2 0) crystal reflections were observed, indicating NiO was converted to Ni species after reduction. Besides, Ni/BEA exhibits a larger FWHM compared to Ni/MOR, Ni/NZ and Ni/Escott, suggesting the generation of smaller Ni species in Ni/BEA, which is consistent with the results obtained from chemisorption (as summarised in Table 1). The heulandite, SiO_2 and potassium aluminium silicate reflections were also observed in Escott natural zeolite. In contrast, chabazite, mordenite, SiO_2 and sanidine diffraction patterns are detected in NZ natural zeolite. A high intensity of SiO_2 reflections was observed in the Escott zeolite compared to NZ, suggesting a high concentration of SiO_2 is present in the Escott zeolite which leads to a lower micropore volume due to the lack of

Published on 14 June 2021. Downloaded on 8/31/2021 9:38:13 PM.

Table 1 Physicochemical properties of the supports and catalysts used in this study

Catalyst	Ni loading[a] (wt%)	Fe content[a] (wt%)	S-micro[b] ($m^2\ g^{-1}$)	S-meso[c] ($m^2\ g^{-1}$)	Vmicro[b] ($cm^3\ g^{-1}$)	Vmeso[c] ($cm^3\ g^{-1}$)	$d$meso[c] (nm)	D[d] (%)	dNi-chem[e] (nm)
Escott	0	1.0	10	16	0.005	0.03	8.3	—	—
NZ	0	1.0	177	29	0.09	0.05	7.7	—	—
HBEA	0	0	269	175	0.15	0.35	9.0	—	—
HMOR	0	0	349	30	0.18	0.05	6.4	—	—
Ni/Escott	4.5	1.0	4	15	0	0.03	9.1	4.6	13.5
Ni/NZ	4.8	1.0	167	28	0.09	0.03	7.3	6.8	9.0
Ni/BEA	5.3	0	286	162	0.15	0.30	8.1	13.7	4.5
Ni/MOR	5.2	0	335	25	0.18	0.04	5.7	9.7	6.4

[a] By XRF analysis. [b] From N_2 adsorption measurements (t-plot). [c] From N_2 adsorption measurements (BJH method), d_{meso} = the average diameter of mesopores. [d] Metal dispersion, based on CO-chemisorption (eqn (1)). [e] Average Ni particle size, based on chemisorption (eqn (2)).

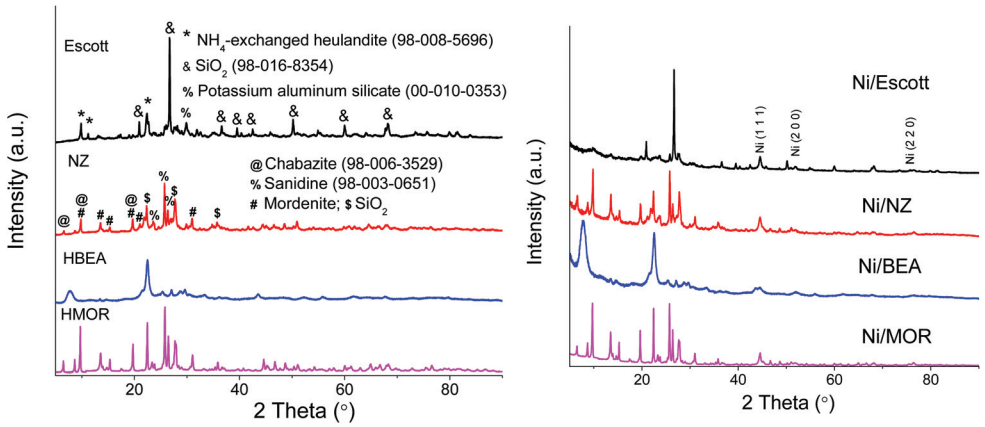

Fig. 1 XRD of supports and pre-reduced Ni/Escott, Ni/NZ, Ni/BEA and Ni/MOR catalysts.

micropores in SiO_2. NZ zeolite was composed of a high concentration of chabazite and mordenite zeolites, which contain a significantly higher concentration of micropores (as shown in Table 1).

HR-TEM experiments were carried out to further investigate the morphology and metal size distribution of pre-reduced Ni/Escott, Ni/NZ and Ni/BEA with results presented in Fig. 2. The grey areas are the image from the zeolite supports and the black dots indicate the presence of Ni particles. The average particle size distribution of Ni/Escott and Ni/NZ was found to range from 6–31 nm. In contrast, the average particle size distribution of Ni/BEA ranges from 3–11 nm, indicating a significant increase in Ni species distribution.

Ni $2p_{3/2}$ spectra of the pre-reduced samples were examined by X-ray photoelectron spectroscopy (XPS) with the profiles presented in Fig. 3. The position of Ni 2p XPS spectra can be influenced by the local chemical environment and shift to higher binding energy (lower kinetic energy due to strong Coulomb interaction of the photoelectron) when the charge density of the Ni decreases.[35] The Ni $2p_{3/2}$ binding energy of Ni/Escott and Ni/NZ was observed at 853.6 eV and 853.4 eV respectively, which is attributed to Ni^{2+}.[36] Compared to Ni/Escott, the Ni $2p_{3/2}$ binding energy of Ni/BEA and Ni/MOR displays a positive shift by 1.2 eV, indicating the smaller Ni species possess a strong interaction with BEA and MOR which allows the electrons transfer from Ni to supports.

The temperature-programmed desorption of ammonia (NH_3-TPD) and ammonia FTIR spectra for the pre-reduced catalysts are displayed in Fig. 4. As shown in Fig. 4a, Ni/MOR exhibits the highest concentration of acid sites, followed by Ni/NZ, Ni/BEA and Ni/Escott. The Ni/MOR and Ni/BEA displayed the majority of NH_3 desorption occurs around 405 °C and 285 °C, respectively, while the natural zeolites (Fig. S2‡) and catalysts presented a lower desorption temperature (~250 °C), suggesting the natural zeolites contain weak acid sites with the heats of desorption summarised in Table S1.‡ The main desorption peak of catalysts can be ascribed to the Brønsted acid sites. To confirm this assumption, IR spectra obtained from adsorption of NH_3 on Ni/NZ, Ni/Escott, Ni/BEA and Ni/MOR were recorded with results displayed in Fig. 4b. The adsorption of NH_3 on all samples exhibits two main bands in the range of 1370–1507 cm^{-1} and 1563–1700 cm^{-1}. The band centred around 1450 cm^{-1} accounts for the vibrations of NH_4^+, which was formed by NH_3 molecules reacting with Brønsted acid sites and coordinated to the zeolite framework.[37,38] Based on band areas, the Ni/MOR catalyst possessed the highest concentration of Brønsted acid sites, followed by the Ni/BEA, Ni/NZ and Ni/Escott. The Ni/Escott exhibits the lowest quantity of

 This journal is © The Royal Society of Chemistry 2021

Published on 14 June 2021. Downloaded on 8/31/2021 9:38:13 PM.

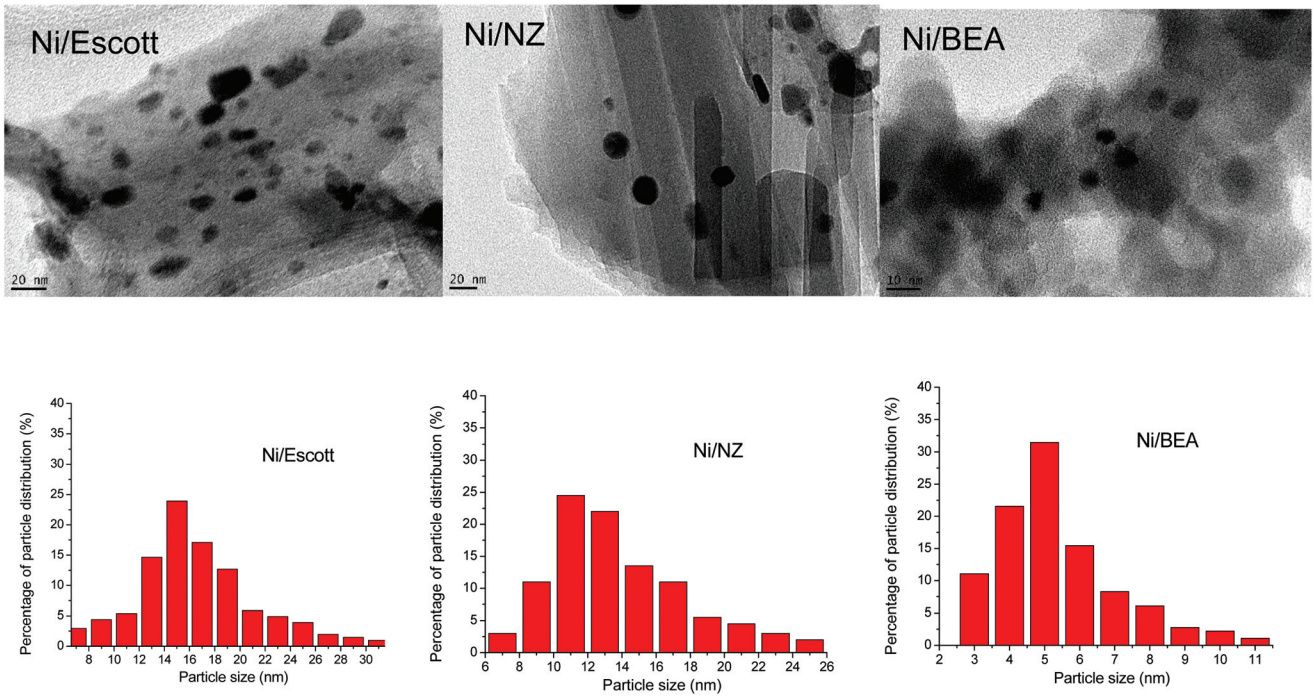

Fig. 2 TEM images and particle distributions of pre-reduced Ni/Escott, Ni/NZ and Ni/BEA. Note the differing scales used in the HR-TEM Ni/BEA image (10 nm) compared to the HR-TEM Ni/Escott and Ni/NZ images (20 nm).

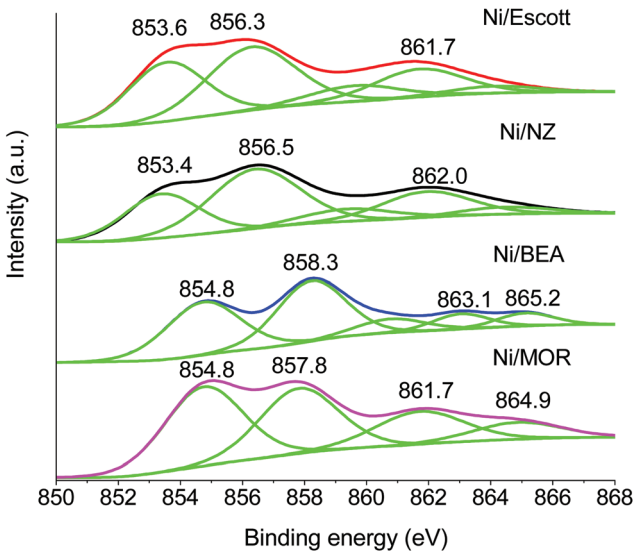

Fig. 3 Ni $2p_{3/2}$ spectra of pre-reduced Ni/Escott, Ni/NZ, Ni/BEA and Ni/MOR catalysts.

acid sites which could be attributed to its lower concentration of micropores as compared to Ni/MOR, Ni/NZ and Ni/BEA. The band centred at 1620 cm^{-1} can be ascribed to symmetric bending vibrations of NH_3 coordinated to Lewis acid sites (Al^{3+}, Ni^{2+}).[39,40] In addition, it is noted the intensity of vibrations at 1620 cm^{-1} over pre-reduced Ni/BEA was significantly enhanced compared to the parent HBEA (Fig. S3‡), which could be attributed to the re-oxidization of part metallic Ni species during the wafer preparation, forming Lewis cationic Ni sites.[8]

The differential NH_3-FTIR band areas extracted from 1370–1507 cm^{-1} (Brønsted acid sites) of Ni/NZ and Ni/BEA as a function of temperature are plotted in Fig. 4c and d respectively. It shows the majority of NH_4^+ vibrations decrease at 246 °C and 290 °C for Ni/NZ and Ni/BEA, respectively, relating to the main peaks in NH_3-TPD (Fig. 4d), suggesting the main NH_3 desorption peaks in NH_3-TPD profiles are attributed to the Brønsted acid sites.

H_2-TPR profiles of catalysts are displayed in Fig. 5. Two main reduction peaks are detected over all catalysts. The low-temperature H_2 consumption peak (centred around 412–440 °C), which is the dominant reduction peak observed over Ni/Escott catalyst, can be assigned to the reduction of bulk Ni nanoparticles presented on the zeolite external surface and some mesopores.[8,41] In our previous studies, the low-temperature reduction peak appeared in catalysts with an average Ni particle size larger than 1.6 nm.[8] The low-temperature H_2 consumption zone (~400 °C) was also observed over ZSM-5 and SiO_2 supported Ni,[42,43] which contributed to the reduction of NiO nanoparticles possessed weak interaction with support.

In contrast, the Ni/BEA and Ni/MOR exhibit the main high-temperature reduction peak (562 °C, 541 °C) relating to smaller Ni particles that are characterised by strong metal–support interaction.[15,43] In addition, the reduction temperature for the smaller Ni species over Ni/MOR, Ni/BEA and Ni/NZ catalysts is higher than that of Ni/Escott, which could be attrib-

Published on 14 June 2021. Downloaded on 8/31/2021 9:38:13 PM.

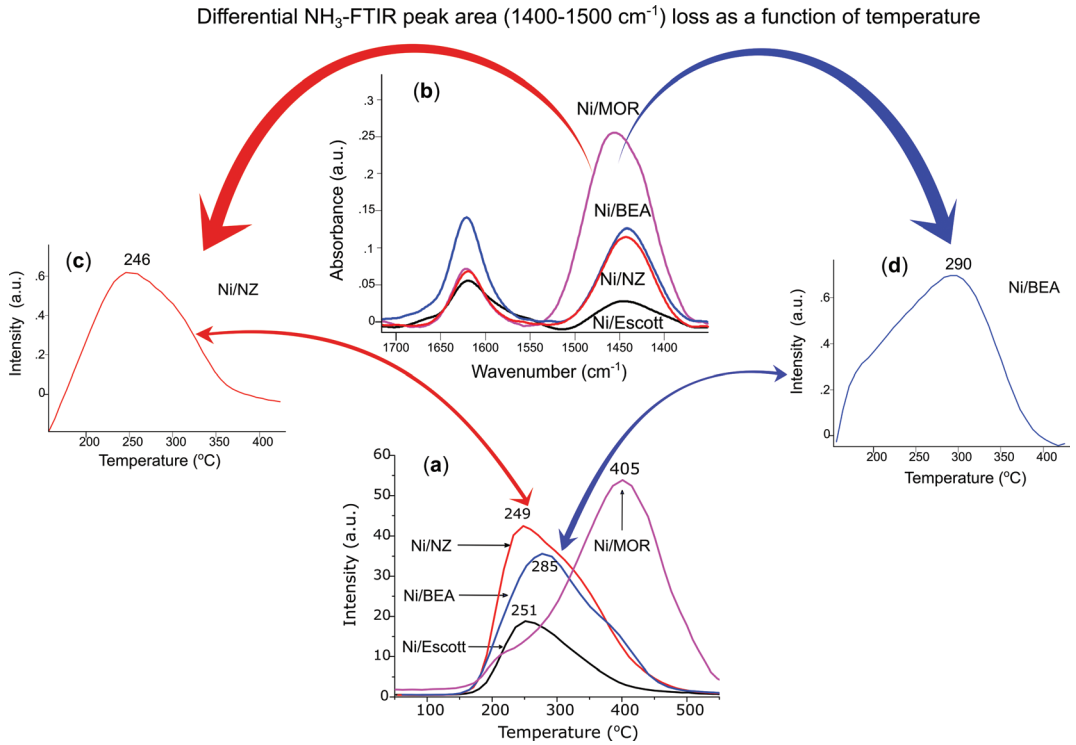

Fig. 4 (a) NH_3-TPD profiles of pre-reduced samples; (b) infrared spectra were obtained from adsorption of ammonia in pre-reduced Ni/Escott, Ni/NZ, Ni/BEA and Ni/MOR, samples contacted with 10 mbar pressure of NH_3 at 150 °C then were vacuumed; the spectra were normalised for wafer thickness using overtones of lattice vibrations between 1556 cm^{-1} and 2105 cm^{-1}; differential NH_3-FTIR peak area loss of (c) Ni/NZ (1400–1500 cm^{-1}) and (d) Ni/BEA (1400–1500 cm^{-1}) as a function of temperature (10 °C min^{-1}).

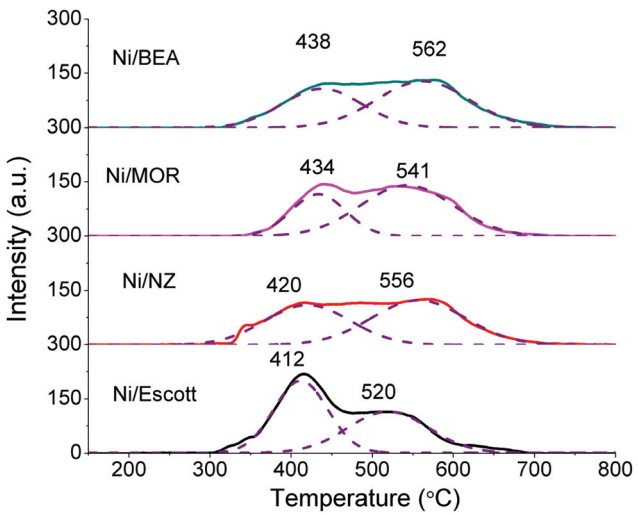

Fig. 5 H_2-TPR profiles of calcined Ni/BEA, Ni/MOR, Ni/NZ and Ni/Escott catalysts.

uted to the Ni species being formed in the micropores of Ni/MOR, Ni/BEA and Ni/NZ engendering a stronger interaction with support. In contrast, the Ni/Escott has larger pores and bigger Ni particles, which may reduce the strength of the metal–support interaction. Escott and NZ both exhibit a small peak around 562 °C even without Ni loading (Fig. S4‡), attributed to the reduction of Fe oxides contained in natural zeolites as indicated by XRF.

H_2-TPD and H_2-FTIR experiments were carried out in order to investigate the H_2 desorption activity of catalyst, with profiles displayed in Fig. 6. The original supports do not exhibit desorbed H_2 as shown in Fig. S5,‡ indicating the Fe atoms presented in the natural zeolites do not possess H_2 adsorption activity.

All catalysts present a high concentration of desorbed H_2 following Ni loading and subsequent reduction to metallic species (as indicated in Fig. 6a). The H_2-TPD profiles were fitted by mixed Gaussian–Lorentzian function with the concentration of desorbed H_2 over various temperature ranges summarised in Table 2. Ni/BEA and Ni/MOR exhibit a primary H_2 desorption peak around 150 °C with a small peak around 212–226 °C. In contrast, a large H_2 desorption peak centred around 211 °C and a small low-temperature desorption peak (154 °C) are observed over Ni/Escott. The second derivative function was applied in differentiating the H_2-TPD profiles of the pre-reduced catalysts (as shown in Fig. S6‡). In line with fitted profiles of the H_2-TPD, the Ni/BEA and Ni/MOR display the majority of desorbed H_2 at temperature around 143 °C, corresponding to the main desorption fitted peak at 150 °C (Fig. 6a). Ni/NZ show two major peaks located at 139 °C and 231 °C respectively, relating to the two desorption peaks at 147 °C and 222 °C in Fig. 6a.

 This journal is © The Royal Society of Chemistry 2021

Published on 14 June 2021. Downloaded on 8/31/2021 9:38:13 PM.

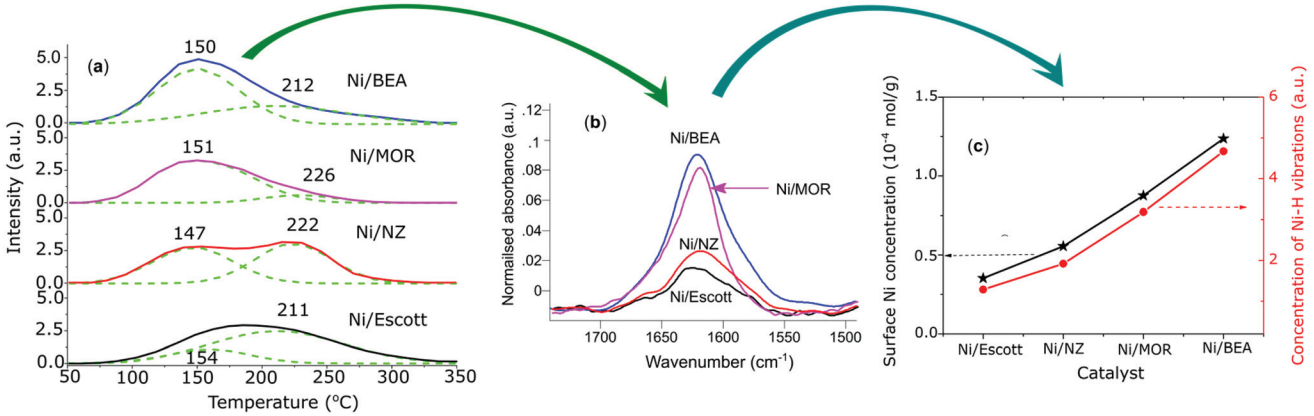

Fig. 6 (a) H_2-TPD and (b) H_2-FTIR profiles of pre-reduced catalysts, the spectra were normalised for wafer thickness using overtones of lattice vibrations between 1556 cm^{-1} and 2105 cm^{-1} in the first spectrum without gas adsorption; (c) the relationship of surface Ni (Ni loading × dispersion) and the peak area of Ni–H vibrations (peak area was derived from 1500–1700 cm^{-1}).

Table 2 Relative quantity of desorbed H_2 in different temperature ranges[a]

	Low temperature (~150 °C) (a.u.)	High temperature (~210 °C) (a.u.)
Ni/Escott	84	316
Ni/NZ	214	226
Ni/BEA	424	77
Ni/MOR	300	41

[a] Based on the peak area in H_2-TPD profiles (Fig. 6a); the peaks were fitted by mixed Gaussian–Lorentzian function; 0.2 g pre-reduced samples were used in the experiments.

The low-temperature desorption peak could be attributed to hydrogen species weakly chemisorbed on the surface of small Ni species.[44–46] A significantly higher concentration of low-temperature desorbed H_2 was observed in Ni/BEA and Ni/MOR compared to Ni/NZ and Ni/Escott, which could be attributed to the higher concentration of surface Ni species. While Ni/Escott exhibits a lower concentration of desorbed H_2 in the low-temperature region, it shows a significantly higher concentration of high-temperature desorbed H_2 compared to Ni/BEA. Besides, the Ni/NZ displays a higher low-temperature H_2 desorption peak area compared to Ni/Escott, which can be attributed to the high amount of micropores in NZ facilitating the formation of small Ni species which weakly chemisorb the H species on the metal surface.

The surface H species are also characterised by H_2-FTIR as presented in Fig. 6b. The IR band at 1620 cm^{-1} observed in pre-reduced Ni catalysts (absent in calcined catalysts) could be attributed to the dissociative chemisorbed H species, *e.g.* Ni–H.[44,47] The Ni/BEA displays the highest amount of surface Ni–H vibrations, followed by Ni/MOR, Ni/NZ and Ni/Escott, which is well in line with the peak area sequence of low-temperature desorbed H_2 (as shown in Fig. 6a). The relationship of surface Ni concentration (Ni loading × dispersion) and the intensity of Ni–H vibrations (peak area derived from 1500–1700 cm^{-1}) is displayed in Fig. 6c. The concentration of Ni–H vibrations increases with the increasing surface Ni, suggesting the Ni–H vibrations are formed mainly depending on the number of surface Ni sites. While Ni/NZ and Ni/Escott presented a higher amount of high-temperature desorbed H_2, a lower concentration of Ni–H vibrations was observed, suggesting the H species that were strongly adsorbed by the bulk Ni did not form the invisible Ni–H vibrations. Since the H absorbed in bulk Ni is desorbed at very low temperature (<0 °C),[45,48] the high-temperature desorbed H_2 could be attributed to the layer of chemisorbed hydrogen between the Ni particles and support or remote from the Ni clusters, *i.e.*, hydrogen species on the support.[45,49] While Ni/MOR exhibits a lower dispersion and larger average Ni particle size compared to Ni/BEA, a lower concentration of high-temperature desorbed H_2 (as shown in Table 2) was observed, which could be attributed to the partial blockage of two-dimensional micropores in Ni/MOR.

3.2. Results of hydrogenation and HDO experiments

3.2.1. Hydrogenation of toluene. Hydrogenation of toluene over the prepared catalysts was carried out to investigate the catalyst hydrogenation activity, with performance results summarised in Table 3. The hydrogenation activity of catalyst mainly depends on Ni properties (such as metal dispersion and particle size), and catalysts with a high metal dispersion commonly exhibit an improved hydrogenation activity.[50,51] Ni/Escott, however, owing to the lowest Ni dispersion, exhibits the highest yield of methylcyclohexane, followed by Ni/NZ, Ni/BEA and Ni/MOR, indicating a higher hydrogenation activity possessed by natural zeolite supported Ni catalysts.

While Ni/BEA exhibits a significantly higher concentration of surface Ni compared to Ni/NZ and Ni/Escott, a lower methylcyclohexane formation rate was observed. Ni/BEA and Ni/MOR show a high concentration of desorbed H_2 as well as Ni/NZ and Ni/Escott (as presented in Fig. 6 and Table 2), however, the majority of H species were weakly adsorbed on Ni surface

Published on 14 June 2021. Downloaded on 8/31/2021 9:38:13 PM.

Table 3 Conversion and yield of hydrogenation of toluene[a]

Catalyst	X-toluene (%)	Y-methylcyclohexane (%)	Y-others[b] (%)	r-methylcyclohexane[c]
Ni/Escott	21.8	20.9	0.4	6.5
Ni/NZ	15.2	13.2	1.7	4.1
Ni/BEA	9.2	4.8	3.8	1.4
Ni/MOR	4.5	2.2	2.1	0.6
Escott	0	0	0	0
NZ	0	0	0	0
BEA	0	0	0	0
MOR	0	0	0	0

[a] Reaction conditions: Catalyst (0.05 g), WHSV (3.05 min^{-1}); P_{H_2} (4.0 MPa), temperature (220 °C), H_2 flow rate (150 mL min^{-1}), liquid flow rate (0.153 g min^{-1}). [b] Others include cyclohexene, ethyl-cyclopentane, (methylcyclohexyl)-toluene. [c] r-methylcyclohexane = methylcyclohexane formation rate per gram catalyst per minute, and the rate is an average over 20–40 min, unit (10^{-3} $mol_{methylcyclohexane}$ g_{cat}^{-1} min^{-1}).

which were desorbed at a lower temperature (~150 °C). Therefore, Ni/BEA and Ni/MOR display a lower methylcyclohexane formation rate at reaction temperature of 220 °C as the concentration of active H species on charge compensating Ni was low under reaction conditions. As a result, the low-temperature H species weakly adsorbed by small Ni particles play a limited role in the hydrogenation of toluene. In comparison, the Ni/Escott displays the majority of desorbed H_2 at a higher temperature (~211 °C), the active H species remained on the large Ni particles during the reaction and facilitated the hydrogenation reactions.

The rate of formation of methylcyclohexane, based on the number of H_2 desorbed sites (low temperature, high-temperature, and the sum of both) (as summarised in Table 2), is presented in Fig. 7 to correlate the desorbed H_2 and the reaction rate. A similar (normalised) methylcyclohexane formation rate was observed over Ni/Escott, Ni/NZ, Ni/BEA and Ni/MOR when the methylcyclohexane formation rate was normalised by the high-temperature desorbed H_2 sites, indicating the strong adsorption/desorption H sites on the larger Ni nanoparticles play a crucial role in the hydrogenation reactions.

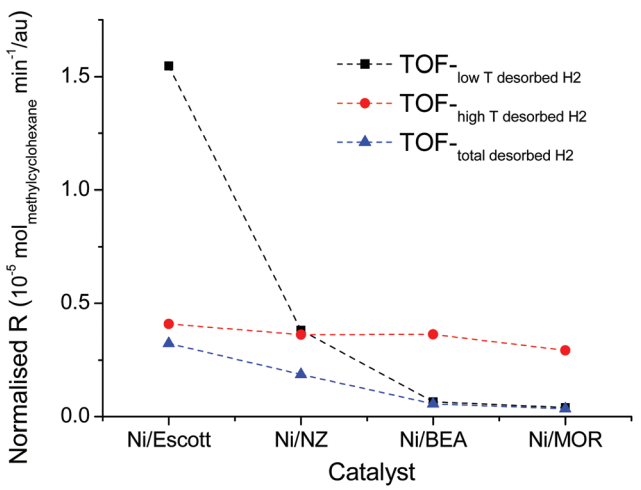

Fig. 7 Normalised methylcyclohexane formation rate for Ni/Escott, Ni/NZ, Ni/BEA and Ni/MOR; TOF-low T desorbed H_2 = methylcyclohexane formation rate based on the number of low-temperature H_2 desorbed sites, TOF-$_{high\ T\ desorbed\ H_2}$ = methylcyclohexane formation rate based on the number of high-temperature H_2 desorbed sites, TOF-$_{total\ desorbed\ H_2}$ = methylcyclohexane formation rate based on the sum of low-temperature and high-temperature H_2 desorbed sites, (the number of H_2 desorbed sites was summarised in Table 2).

In addition, toluene was not activated by pre-reduced supports, suggesting the acid sites and Fe species cannot catalyse the hydrogenation of toluene, and thus Ni species are the active sites.

The pore size of supports has a significant impact on the activity and stability of catalysts in the HDO reactions.[52,53] Catalysts with high concentration of mesopores sometimes provide an enhanced activity for large-size molecules present in biocrude oils due to a less pronounced diffusion limitation.[6,13] In this study, Ni/MOR and Ni/NZ catalysts display a high concentration of micropores and few mesopores, while a similar TOF-$_{high\ T\ desorbed\ H_2}$ was detected over all catalysts, indicating there was no significant diffusion limit for toluene in the micropores. The internal pore diameter of MOR is 6.7 Å,[6] which is larger than the kinetic diameter of toluene (5.68–5.85 Å),[54–56] therefore, the entrance and diffusion of toluene in the micropores of MOR is less restricted.

3.2.2. Hydrodeoxygenation of anisole. The natural zeolites supported Ni catalysts possess a higher hydrogenation activity compared to Ni/BEA in the hydrogenation of toluene. The HDO reactions in contrast require metal sites as well as acid sites for hydrogenation and deoxygenation. Anisole (a model compound of biocrude oil) was employed to investigate the HDO activity of catalysts, with performance results summarised in Table 4.

While methylcyclohexane formation rate over Ni/Escott in hydrogenation of toluene is 4.6 and 10.8 times higher than that of Ni/BEA and Ni/MOR, respectively, the cyclohexane formation rate of Ni/Escott in HDO of anisole is only 2.2 and 3.4 times higher than Ni/BEA and Ni/MOR, respectively, indicating the high concentration of Brønsted acid sites in Ni/BEA and Ni/MOR facilitates the HDO reaction. The normalised cyclohexane formation rates based on the peak area of high-temperature desorbed H_2 (TOF-$_{high\ T\ desorbed\ H_2}$) and concentration of Brønsted acid sites (TOF-$_B$) are depicted in Fig. 8. The Ni/Escott exhibits the highest TOF-$_B$, followed by Ni/NZ, Ni/BEA and Ni/MOR, however, this order is reversed when cyclohexane production rate is normalised by the peak area of high-temperature desorbed H_2, suggesting acid and metal sites both promote the HDO of anisole to cyclohexane.

A significantly enhanced selectivity of methylanisole was observed in Ni/BEA as compared to Ni/Escott, Ni/NZ and Ni/MOR. The formation of methylanisole can be attributed to the transalkylation of anisole *via* acid sites, as reported by literature[20,57] and confirmed by the performance results of pure HBEA (Table S2,‡ phenol and methylanisole were the main products). The surface Ni was also reported to facilitate the transalkylation.[19] As a result, the transalkylation of anisole to methylanisole and phenol was promoted by the strong

 This journal is © The Royal Society of Chemistry 2021

Published on 14 June 2021. Downloaded on 8/31/2021 9:38:13 PM.

Table 4 HDO of anisole over Ni/Escott, Ni/NZ, Ni/BEA and Ni/MOR catalysts[a]

Catalyst	Total acid con.[b] (mmol g_{cat}^{-1})	B^c (mmol g_{cat}^{-1})	$X_{anisole}$ (%)	$S_{cyclohexane}$ (%)	$S_{benzene}$ (%)	$S_{methylanisole}$ (%)	$S_{1,1'\text{-bicyclohexyl}}$ (%)	$S_{cyclohexyl\text{-}anisole}$ (%)	$S_{(methylcyclohexyl)anisole}$ (%)	S_{others}^d (%)	$r_{cyclohexane}^e$
Ni/Escott	0.22	0.15	28.9	57.4	4.5	2.1	4.5	18.3	0.7	11.4	2.4
Ni/NZ	0.57	0.38	33.6	44.0	3.6	3.6	4.5	30.7	2.1	10.1	2.1
Ni/BEA	0.49	0.41	18.8	40.0	3.7	14.4	3.2	14.9	8.5	9.0	1.1
Ni/MOR	0.88	0.85	13.5	34.1	2.2	4.1	1.8	39.3	2.3	8.1	0.7

[a] Reaction conditions: Reaction temperature (230 °C), catalyst (0.1 g), WHSV (1.2 min^{-1}), P_{H_2} (4.0 MPa), H_2 flow rate (150 mL min^{-1}), liquid flow rate (0.12 g min^{-1}). [b] The total acid concentration was calculated by NH_3-TPD. [c] The concentration of Brønsted acid was calculated by NH_3-FTIR. [d] Others include methane and cyclohexene. [e] $r_{cyclohexane}$ = cyclohexane formation rate per catalyst per minute, and the rate is an average over the 20–40 min, unit (10^{-3} $mol_{cyclohexane}$ g_{cat}^{-1} min^{-1}).

Fig. 8 Normalised cyclohexane formation rate for Ni/Escott, Ni/NZ, Ni/BEA and Ni/MOR catalysts; $TOF\text{-}_B$ = cyclohexane formation rate based on the concentration of Brønsted acid sites, $TOF\text{-}_{high\ T\ desorbed\ H_2}$ = cyclohexane formation rate based on the peak area of high-temperature desorbed H_2.

Brønsted acid sites and high concentration of surface Ni of Ni/BEA. The phenol was absent in the products, which could be attributed to the fast hydrogenolysis of phenol to benzene *via* the surface Ni species, and the formed benzene was hydrogenated to cyclohexane *via* the active H species. The phenol was more easily activated by zeolite supported Ni catalyst compared to anisole and toluene in HDO of a mixed feedstock.[53]

Based on above experiment results and research published elsewhere, the proposed reaction pathways for the HDO of anisole over BEA, MOR and natural zeolites supported Ni catalysts are summarised in Scheme 1. The anisole is hydrogenated to methoxycyclohexane (R1) *via* the active H species, followed by the demethoxylation of methoxycyclohexane to cyclohexene *via* the Brønsted acid sites (R2), which is the main reaction pathway over bifunctional catalysts with Ni nanoparticles and high H_2 pressure.[21,58] The Lewis acid sites have a negligible activity in deoxygenation of methoxycyclohexane.[13]

In addition, the anisole can also undergo transalkylation *via* acid sites to form methylanisole and phenol (R3), followed by the hydrogenolysis of phenol (fast step, R5) and methylanisole (slow step, R6) to benzene and toluene *via* the charge-compensating Ni species which contain a low amount of active H species at 230 °C. The alkylation reactions *via* the acid sites was also observed in previous studies.[8,20,57,59] The formed benzene and toluene are hydrogenated to cyclohexene and methylcyclohexene. Due to the high amount of surface Ni and high concentration of strong Brønsted acid sites, transalkylation and hydrogenolysis (R3, R5) are significantly promoted *via* the Ni/BEA catalyst, leading to a higher selectivity of methylanisole compared to Ni/NZ and Ni/Escott (as shown in Table 4). Benzene was observed to be the main product without further hydrogenation over Ni-based catalysts in some previous studies,[20,59,60] which could be attributed to the

Published on 14 June 2021. Downloaded on 8/31/2021 9:38:13 PM.

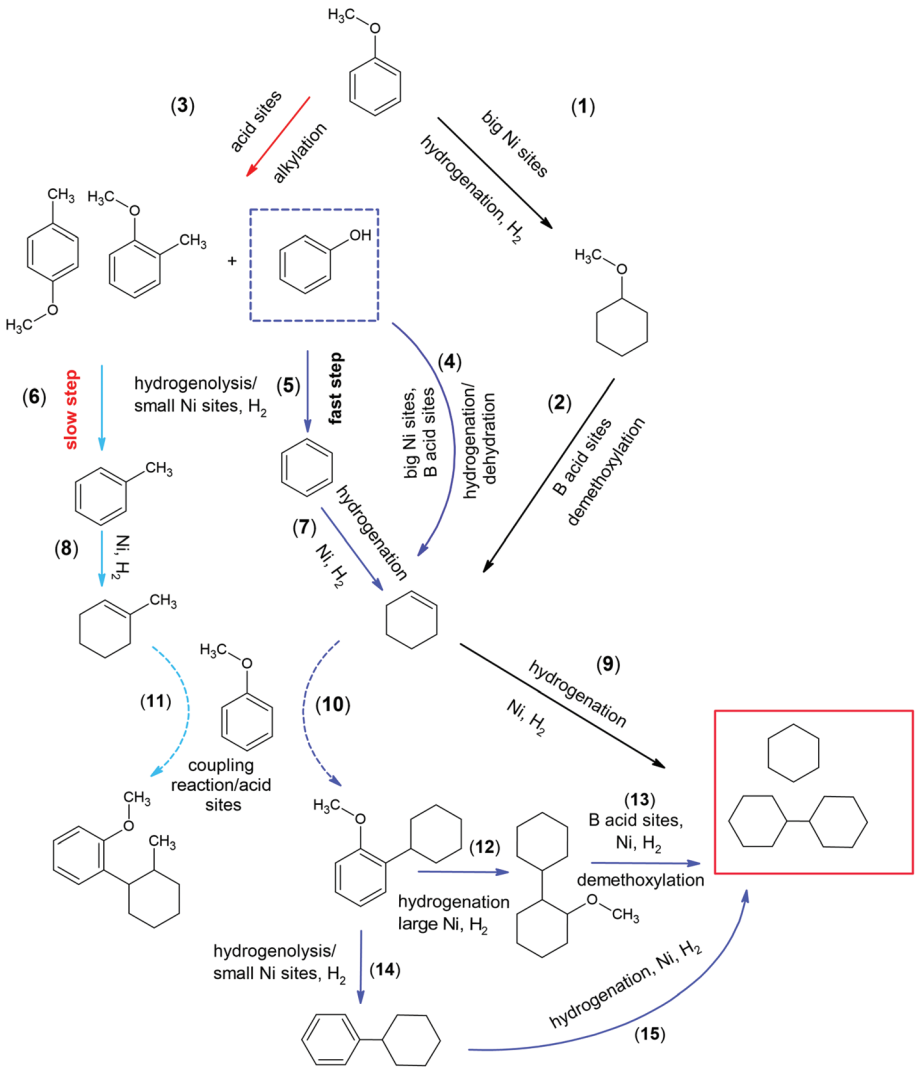

Scheme 1 Proposed reaction pathways for HDO of anisole over Ni/Escott, Ni/NZ, Ni/BEA and Ni/MOR.

atmospheric pressure and higher reaction temperature (300–450 °C) employed in their studies. High H_2 pressure and mild reaction temperature facilitate the full hydrogenation of aromatic rings.[21,52]

The formed cyclohexene is hydrogenated to cyclohexane (R9) which is the primary final product. Besides, the cyclohexene and methylcyclohexene can also react with anisole to form cyclohexylanisole (R10) and methylcyclohexylanisole (R11) *via* the acid sites.[8] The formed cyclohexylanisole undergoes two reaction pathways (R12 and 13: hydrogenation–demethoxylation and R14 and 15: hydrogenolysis–hydrogenation) to 1,1′-bicyclohexyl based on the Ni species contained in catalysts. The formation of C–C coupling products facilitated by catalysts with high acidity was also observed by other studies.[21,61,62] The presence of protons is the main reason for the production of coupling products (bicyclohexyl, cyclohexyl-anisole, *etc.*).[53,61,63,64]

To summarise, the natural zeolites supported Ni catalysts exhibit desirable HDO and hydrogenation activities compared to Ni/BEA and Ni/MOR catalysts. Moreover, natural zeolites are extremely cheaper and abundant compared to synthetic zeolites. Therefore, the natural zeolites supported Ni catalysts have a great potential to be widely used in industrial hydrotreating reactors.

4. Conclusions

Natural zeolites supported Ni catalysts were employed for the HDO/hydrogenation reactions. Ni/Escott and Ni/NZ exhibit a significantly higher hydrogenation activity in the hydrogenation of toluene compared to Ni/BEA and Ni/MOR due to their high concentration of active H species which were dissociative adsorbed by bulk Ni particles and desorbed at a higher temperature (210–220 °C). The strongly chemisorbed H species promote the hydrogenation of toluene at the reaction temperature of 220 °C. While Ni/BEA and Ni/MOR exhibit a higher metal dispersion, the smaller Ni species possess a stronger metal–support interaction, leading to a higher concentration

 This journal is © The Royal Society of Chemistry 2021

Published on 14 June 2021. Downloaded on 8/31/2021 9:38:13 PM.

of weakly chemisorbed H species which were desorbed around 150 °C. Also, the Ni/Escott and Ni/NZ exhibit a higher HDO activity compared to Ni/BEA and Ni/MOR in the HDO of anisole due to their high hydrogenation activity. The high concentration of strong Brønsted acid sites and large number of surface Ni sites in Ni/BEA enhanced the transalkylation of anisole to phenol and hydrogenolysis of phenol to benzene, followed by the hydrogenation of benzene to cyclohexane, leading to a relatively improved HDO activity compared to its hydrogenation activity.

Conflicts of interest

There are no conflicts to declare.

Acknowledgements

Authors thanks the Zeolite Australia Limited for providing the natural zeolites. Funding from the Australian Research Council is gratefully acknowledged. Authors thank the Electron Microscope and X-ray Unit of the University of Newcastle for the use of their facilities.

References

1 C. Liu, H. Wang, A. M. Karim, J. Sun and Y. Wang, *Chem. Soc. Rev.*, 2014, **43**, 7594.
2 Y. Mathieu, L. Sauvanaud, L. Humphreys, W. Rowlands, T. Maschmeyer and A. Corma, *ChemCatChem*, 2017, **9**, 1574.
3 D. D. Laskar and B. Yang, *Biofuels, Bioprod. Biorefin.*, 2013, **7**, 602.
4 D. R. Vardon, B. K. Sharma, J. Scott, G. Yu, Z. C. Wang, L. Schideman, Y. H. Zhang and T. J. Strathmann, *Bioresour. Technol.*, 2011, **102**, 8295.
5 H. Wang, H. Ruan, H. Pei, H. Wang, X. Chen, M. P. Tucker, J. R. Cort and B. Yang, *Green Chem.*, 2015, **17**, 5131.
6 P. Yan, G. Bryant, M. M. J. Li, J. Mensah, E. Kennedy and M. Stockenhuber, *Microporous Mesoporous Mater.*, 2020, **309**, 110561–110574.
7 E. Furimsky, *Appl. Catal., A*, 2000, **199**(2), 147.
8 P. Yan, M. M. J. Li, A. A. Adesina, G. Zhao, A. Setiawan, E. M. Kennedy and M. Stockenhuber, *Catal. Sci. Technol.*, 2020, **10**, 810.
9 W. Song, Y. Liu, E. Barath, C. Zhao and J. A. Lercher, *Green Chem.*, 2015, **17**, 1204.
10 Z. Yang, W. Chen, J. Zhang, Z. Yang, N. Zhang, C. Zhong and B. H. Chen, *J. Catal.*, 2018, **363**, 52.
11 M. S. Zanuttini, C. D. Lago, M. S. Gross, M. A. Peralta and C. A. Querini, *Ind. Eng. Chem. Res.*, 2017, **56**, 6419.
12 L. Nie and D. E. Resasco, *J. Catal.*, 2014, **317**, 22.
13 P. Yan, J. Mensah, M. Drewery, E. Kennedy, T. Maschmeyer and M. Stockenhuber, *Appl. Catal., B*, 2021, **281**, 119470.
14 L. Zhou and A. Lawal, *Catal. Sci. Technol.*, 2016, **6**, 1442.
15 P. Yan, J. Mensah, A. Adesina, E. Kennedy and M. Stockenhuber, *Appl. Catal., B*, 2020, **267**, 118690.
16 C. Zhao and J. A. Lercher, *Angew. Chem.*, 2012, **124**, 6037.
17 X. Liu, W. An, C. H. Turner and D. E. Resasco, *J. Catal.*, 2018, **359**, 272.
18 Y. Zheng, N. Zhao and J. Chen, *Appl. Catal., B*, 2019, **250**, 280.
19 H. Wang, M. Feng and B. Yang, *Green Chem.*, 2017, **19**, 1668.
20 X. Xu, E. Jiang, Z. Li and Y. Sun, *Fuel*, 2018, **221**, 440.
21 D. P. Gamliel, B. P. Baillie, E. Augustine, J. Hall, G. M. Bollas and J. A. Valla, *Microporous Mesoporous Mater.*, 2018, **261**, 18.
22 S. Xu, A. Zheng, Y. Wei, J. Chen, J. Li, Y. Chu, M. Zhang, Q. Wang, Y. Zhou, J. Wang, F. Deng and Z. Liu, *Angew. Chem.*, 2013, **125**, 11778.
23 G. Bonilla, I. Diaz, M. Tsapatsis, H. K. Jeong, Y. Lee and D. G. Vlachos, *Chem. Mater.*, 2004, **16**, 5697.
24 A. S. M. Junaid, C. Street, W. Wang, M. M. Rahman, W. An, W. C. McCaffrey and S. M. Kuznicki, *Fuel*, 2012, **94**, 457.
25 R. H. Ibrasheva and K. A. Zhubanov, *Stud. Surf. Sci. Catal.*, 2000, **130**, 2447.
26 J. E. Sánchez-Velandia, J. F. Gelves, L. Dorkis, M. A. Márquez and A. L. Villa, *Microporous Mesoporous Mater.*, 2019, **287**, 114.
27 O. Akpolat, G. Gunduz, F. Ozkan and Nu. Besün, *Appl. Catal., A*, 2004, **265**, 11.
28 Q. Han, M. U. Rehman, J. Wang, A. Rykov, O. Y. Gutierrez, Y. Zhao, S. Wang, X. Ma and J. A. Lercher, *Appl. Catal., B*, 2019, **253**, 348.
29 H. Fang, J. Zheng, X. Luo, J. Du, A. Roldan, S. Leoni and Y. Yuan, *Appl. Catal., A*, 2017, **529**, 20.
30 S. Velu and S. K. Gangwal, *Solid State Ionics*, 2006, **177**, 803.
31 A. Borodzinski and M. Bonarowska, *Langmuir*, 1997, **13**, 5613.
32 M. L. M. Bonati, R. W. Joyner and M. Stockenhuber, *Catal. Today*, 2003, **81**, 653.
33 P. A. Redhead, *Vacuum*, 1962, **12**, 203.
34 K. Gora-Marek, K. Brylewska, K. A. Tarach, M. Rutkowska, M. Jablonsa, M. Choi and L. Chmielarz, *Appl. Catal., B*, 2015, **179**, 589.
35 O. Mazaheri and R. J. Kalbasi, *RSC Adv.*, 2015, **5**, 34398.
36 M. O. de Souza, F. M. T. Mendes, R. F. de Souza and J. H. Z. dos Santos, *Microporous Mesoporous Mater.*, 2004, **69**, 217.
37 J. Valyon, G. Onyestyak and L. V. C. Rees, *J. Phys. Chem. B*, 1998, **102**, 8994.
38 F. Yin, A. L. Blumenfeld, V. Gruver and J. J. Fripiat, *J. Phys. Chem. B*, 1997, **101**, 1824.
39 A. Martinez, M. A. Arribas, P. Concepcion and S. Moussa, *Appl. Catal., A*, 2013, **467**, 509.
40 C. Minchev, S. A. Zubkov, V. Valtchev, V. Minkov, N. Micheva and V. Kanazirev, *Appl. Catal., A*, 1994, **119**, 195.
41 J. van de Loosdrecht, A. M. van der Kraan, A. J. van Dillen and J. W. Geus, *J. Catal.*, 1997, **170**, 217.

Published on 14 June 2021. Downloaded on 8/31/2021 9:38:13 PM.

42 A. J. Maia, B. Louis, Y. L. Lam and M. M. Pereira, *J. Catal.*, 2010, **269**, 103.
43 M. Che, Z. Cheng and C. Louis, *J. Am. Chem. Soc.*, 1995, **117**, 2008.
44 S. T. Ceyer, *Acc. Chem. Res.*, 2001, **34**, 737.
45 S. Ewald, S. Standl and O. Hinrichsen, *Appl. Catal., A*, 2018, **549**, 93.
46 L. Znak and J. Zielinski, *Langmuir*, 2006, **22**, 8758.
47 N. A. Eberhardt and H. Guan, *Chem. Rev.*, 2016, **116**, 8373.
48 S. Smeds, T. Salmi, L. P. Lindfors and O. Krause, *Appl. Catal., A*, 1996, **144**, 177.
49 J. T. Miller, B. L. Meyers, M. K. Barr, F. S. Modica and D. C. Koningsberger, *J. Catal.*, 1996, **159**, 41.
50 M. W. Schreiber, D. Rodriguez-Nino, O. Y. Gutiérrez and J. A. Lercher, *Catal. Sci. Technol.*, 2016, **6**, 7976.
51 W. Song, C. Zhao and J. A. Lercher, *Chem. – Eur. J.*, 2013, **19**, 9833.
52 C. Tu, J. Chen, W. Li, H. Wang, K. Deng, V. A. Vinokurov and W. Huang, *Sustainable Energy Fuels*, 2019, **3**, 3462.
53 P. Yan, M. Drewery, J. Mensah, J. C. Makie, E. Kennedy and M. Stockenhuber, *Top. Catal.*, 2020, **63**, 778.
54 J. F. Denayer, W. Souverjins, P. A. Jacobs, J. A. Martens and G. V. Baron, *J. Phys. Chem. B*, 1998, **102**, 458.
55 J. Jae, G. A. Tompsett, A. J. Foster, K. D. Hammond, S. M. Auerbach, R. F. Lobo and G. W. Huber, *J. Catal.*, 2011, **279**, 257.
56 H. Wang and M. Frenklach, *Combust. Flame*, 1994, **96**, 163.
57 X. Zhu, L. L. Lobban, R. G. Mallinson and D. E. Resasco, *J. Catal.*, 2011, **281**, 21.
58 Y. Yang, C. Ochoa-Hernandez, V. A. de La Pena O'Shea, P. Pizarro, J. M. Coronado and D. P. Serrano, *Appl. Catal., B*, 2014, **145**, 91.
59 S. Pichaikaran and P. Arumugam, *Green Chem.*, 2016, **18**, 2888.
60 W. S. Lee, Z. Wang, W. Zheng, D. G. Vlachos and A. Bhan, *Catal. Sci. Technol.*, 2014, **4**, 2340.
61 L. Chen, J. Xin, H. Dong, D. Yan, X. Lu and S. Zhang, *Green Chem.*, 2016, **18**, 2341.
62 E. Furimsky and F. E. Massoth, *Catal. Today*, 1999, **52**, 381.
63 D. Y. Hong, S. J. Miller, P. K. Agrawal and C. W. Jones, *Chem. Commun.*, 2010, **46**, 1038.
64 R. K. M. R. Kallury, T. T. Tidwell, D. G. B. Boocock and D. H. L. Chow, *Can. J. Chem.*, 1984, **62**, 2540.

 This journal is © The Royal Society of Chemistry 2021